A. Zanotti, G. Gibertini
Experimental Assessment of an Active L-Shaped Tab for Dynamic Stall Control
Journal of Fluids and Structures, Vol. 77, 2018, p. 151-169
doi:10.1016/j.jfluidstructs.2017.11.010

Experimental Assessment of an Active L-shaped Tab for Dynamic Stall Control

A. Zanotti[1,*], G. Gibertini[1]

Politecnico di Milano, Dipartimento di Scienze e Tecnologie Aerospaziali
Campus Bovisa, Via La Masa 34, 20156 Milano, Italy

Abstract

An experimental activity was performed on a NACA 23012 pitching airfoil to investigate the effectiveness of an active trailing edge L-shaped tab for deep dynamic stall control. The active control system, based on the use of micro pneumatic actuators, was designed to control the deployment and retraction of the tab along the oscillating cycle. In particular, the tab was designed to behave as a Gurney flap when deployed as its end prong protrudes at the airfoil trailing edge, while in retracted position the tab behaves as a trailing edge flap. The L-shaped tab design presents interesting features to be employed on rotor blades, due to an easier integration at the trailing edge with respect to a deployable Gurney flap. Wind tunnel tests were carried out considering two pitching cycles producing deep dynamic stall regime. Unsteady pressure measurements were performed at the model midspan section to obtain the phase-averaged aerodynamic loads curves. The tests results showed that the deployment of the tab during the upstroke produces a conspicuous increase of lift with respect to the clean airfoil case, corresponding to a higher level of available thrust on the retreating blade. The retraction of the tab before stall onset does not introduce a valuable effect in terms of pitching moment peak reduction with respect to clean airfoil. Moreover, the active control system produces a conspicuous reduction of the negatively-damped portions of the pitching cycles and of the negative aerodynamic damping peak that could account for stall flutter divergence.

Keywords: Dynamic Stall, Gurney Flap, Pitching Airfoil, Wind Tunnel.

*Corresponding author
Email address: alex.zanotti@polimi.it (A. Zanotti)
[1]Assistant Professor

Nomenclature

α	angle of attack [deg]
α_m	mean angle of attack [deg]
α_a	pitching oscillation amplitude [deg]
$\Xi(t)$	time-resolved aerodynamic damping coefficient
Ξ_{cycle}	cycle-integrated aerodynamic damping coefficient
ω	circular frequency [rad/s]
$A_{C_M}(t)$	time-resolved aerodynamic damping amplitude $= \sqrt{C_M^2 + \tilde{C_M}^2}$
b	airfoil section model span [m]
c	airfoil section model chord [m]
C_L	lift coefficient
C_M	pitching moment coefficient about the airfoil quarter chord
C_p	pressure coefficient
DSV	Dynamic Stall vortex
f	oscillation frequency [Hz]
h	height of the deployed L-tab end prong below the trailing edge [m]
HES	Hall Effect Sensor
k	reduced frequency $= \pi f c/U_\infty$
M	Mach number
Re	Reynolds number
t	time [s]
U_∞	free-stream velocity [m/s]
x	chord-wise coordinate axis
Superscripts:	
$\tilde{}$	Hilbert transformed data-series

1. Introduction

In recent years, the strong demand for faster helicopters spurred rotorcraft research activity into retreating blade dynamic stall (McCroskey, 1981) which is one of the main aerodynamic phenomenon responsible for limitation of the performance of classical helicopter rotor configurations. Dynamic stall produces, in fact, several adverse effects on helicopter performance as the limitation of the forward speed and thrust, high control system loads and a high level of vibrations affecting the helicopter dynamic performance in terms of maneuver capability and handling qualities. Moreover, an important issue related to dynamic stall process is the occurrence of *stall flutter* (Carta, 1967), a single degree of freedom limit cycle oscillation causing blade

structural damage and excessive cabin vibration.

The attention of rotorcraft research was therefore addressed to the design of active blades aimed to alleviate the principal detrimental effects induced by dynamic stall in order to expand the helicopter flight envelope, the vehicle utility and preserve the structural integrity of the rotor blades. Of course, the evaluation of an effective active device to be used on a rotor represents a very challenging activity, taking into account the severe requirements related to its integration on a helicopter blade and the severe operative conditions. Many attractive solutions were investigated in the recent literature. The most of these experimental activities were carried out on oscillating airfoils. This test case presents, in fact, the characteristics of being a simple effective tool to evaluate the potential capabilities of the investigated device before a definite experimental assessment in the real operative conditions of a helicopter rotor blade. In the following a brief analysis of the most interesting activities in this field is given.

Improvements in dynamic stall control were investigated by means of the optimisation of the blade airfoil shape during the pitching cycle. For instance, Chandrasekhara et al. (2004) studied the effect of the drooping on the leading portion of an oscillating airfoil. Tests results showed that the leading edge droop reduces the strength of the dynamic stall vortex (DSV) and consequently produces a reduction of the negative peak pitching-moment together with a net positive aerodynamic damping of the airfoil. Similar results were found in the numerical study by Feszty et al. (2004) investigating the effect of a classical trailing edge flap for dynamic stall alleviation over a pitching airfoil. In particular, the upward deflection of the flap for the duration of about $\frac{1}{3}$ of the airfoil motion period produces a weakening of the DSV responsible for the large negative pitching moments and associated to negative aerodynamic damping. Nevertheless, both the described solutions produced a reduction of the available lift force with respect to the clean airfoil configuration. Moreover, the use of such devices would require a complex mechanical system for the actuation that would introduce an apparent increase of weight to be avoided on a rotor blade subject to high centrifugal forces. On the other hand, a quite simple and effective solution in terms of device integration and actuation system was recently explored by Gardner et al. (2017) that obtained interesting results in terms of dynamic stall hysteresis reduction and pitching moment peak decrease by means of a back-flow flap attached to the suction side of an airfoil with a solid-state hinge and guided by a magnetic actuator.

Similar results were found by Le Pape et al. (2012) and Mai et al. (2008) that investigated the use of a row of deployable vortex generators implemented at the leading edge of an airfoil in both static and dynamic stall conditions. Indeed, the experiments showed that the deployment of vortex generators during the retreating blade side of the rotor disk produces the reduction of the pitching moment peak and the area of the negative damping hysteresis loop, but introduces a not negligible penalty on the lift force. Nevertheless, different compromises on the effect on lift and pitching moment can be achieved by varying the heights and the phase of actuation of the vortex generators.

Blowing devices typically used to delay the static stall were also studied for dynamic stall alleviation.

For instance, Singh et al. (2006) investigated the use of air-jet vortex generators. In this test case, the air blown tangentially at the leading edge of the airfoil produces a delay of the flow separation and of the DSV formation. The DSV was also weakened by the air-jet interaction with a consequent reduction of the pitching moment peak. The air-jet blowing also promotes the reattachment of the flow during the downstroke phase of the motion producing a benefit in terms of net aerodynamic damping. A drawback related to the use of such devices on real helicopter blades could be due to the conspicuous power required for the blowing to make the air-jets effective.

The use of plasma actuators for dynamic stall control was recently investigated by Post and Corke (2006). This experimental study showed that an impulsive actuation of such devices in the phase of the pitching cycle characterised by incipient flow separation produces the formation of vortical structures promoting the mixing of the flow on the airfoil surface and responsible of the stall delay and of an early reattachment of the flow in downstroke motion. Even if they can be considered an attractive solution due to their low weight, low intrusiveness and an easy installation on the airfoil surface, the plasma actuators present important drawbacks related to the high voltage required for their use and to their loss of performance for high flow velocities.

Among all these studies, the interest about the effects of a Gurney flap (Liebeck, 1978) on rotor blades (Kentfield, 1993) has recently grown, as demonstrated by the several works about the study of the potential effect of an active deployable Gurney flap (see, for instance the works by Yeo (2008); Kinzel and Maughmer (2010); Woodgate et al. (2016)). Both experimental and numerical activities agree that the lift enhancement mechanism of a Gurney flap can be useful to improve blade aerodynamic performance (Maughmer and Bramesfeld, 2008; Yee et al., 2007). Indeed, numerical studies report that benefits for rotorcraft performance can be obtained by the use of an active Gurney flap deployed on the retreating side of rotor disk and retracted on the advancing side (Yeo, 2008; Woodgate et al., 2016). Nevertheless, as also sustained by experimental results described in Chandrasekhara et al. (2008), a deployable Gurney flap is not expected to have valuable effect in terms of pitching moment peak reduction as the previously cited leading edge devices because, acting at trailing edge region, it should have a very limited effect of vortical structures typical of the dynamic stall process that are generated by flow separations occurring at leading edge (McCroskey, 1981; Leishman, 2006).

The integration of an active Gurney flap on a rotor blade implicates important feasibility problems, related to the very severe requirement to stow the deployable device at the blade trailing edge. Thus, a L-shaped tab at the blade airfoil trailing edge was investigated at Politecnico di Milano to overcome this limitation. Indeed, the tab design exhibits the capability to behave as a deployable Gurney flap with an easy integration in correspondence of the blade trailing edge position where the flap is more effective (Li et al., 2003). Preliminary numerical (Motta et al., 2017) and experimental studies (Zanotti et al., 2014a) investigated this L-shaped tab in fixed positions. In particular, the work by Motta et al. (2017) shows the results of steady-state computations carried out both at small angle of attacks and in deep stall conditions for

different configurations of the L-shaped tab with several rotations of the movable device. Moreover, this work investigated also the behaviour of such flapped configurations at high Mach numbers. On the other hand, the work by Zanotti et al. (2014a) shows an experimental assessment of the L-shaped tab performed on the same test rig used for the present activity with the device static along the pitching cycle in both deployed and retracted position. Then, a first assessment of the capabilities of an active control system for the L-shaped tab was carried out by some tests performed with a preliminary set up that confirmed the effectiveness of the concept (Pisetta, 2016). Then, the present work describes the results of a comprehensive activity carried out with an improved active system characterised by a more stiff and accurate manufacturing of the L-shaped tab aimed to show the potential benefits on deep dynamic stall effects produced by this active controlled device. During the tests, different duty cycles for the L-shaped tab actuation were considered to evaluate the best performance for dynamic stall control purpose. The aerodynamic loads curves were evaluated by the integration of unsteady pressure measurements carried out on the model midspan contour. The effects on the blade section performance due to the active L-shaped tab were evaluated by the comparison of the airloads curves with respect to the clean airfoil configuration. Moreover, a time-resolved analysis of the aerodynamic damping was performed to account the effect of the active L-tab on the occurrence of conditions that could promote stall flutter divergence.

2. Experimental set up

The experimental activity was carried out at the *S. De Ponte* wind tunnel of Politecnico di Milano. The wind tunnel has a rectangular test section with 1.5 m height and 1 m width. The maximum wind velocity is 55 m/s and the free stream turbulence level is less than 0.1%. The experimental assessment of the active L-shaped tab was performed considering two deep dynamic stall conditions according to the definition of McCroskey (1981), consisting in a sinusoidal pitching cycle characterised by a mean angle of attack of $\alpha_m = 10°$ and 15°, respectively, with constant oscillation amplitude of $\alpha_a = 10°$ and reduced frequency k equal to 0.1. The tests were carried out at a wind tunnel free-stream velocity of 30 m/s, corresponding to a Reynolds number of 6×10^5 and a Mach number of 0.09. The Reynolds number representative of a small-medium size helicopter retreating rotor blade section at about 65% radius in forward flight should be of the order of $1 \cdot 10^6$ ($M = 0.15$). A lower testing speed was chosen in the present test campaign to limit the mechanical stress on the actuation system and to avoid fatigue issues on the model strut. On the other hand, the reduced frequency reproduced in the present tests is representative of a real flight condition. Nevertheless, the Reynolds number of the present tests is not far from a real retreating blade flight condition and the comparison with the airloads curves measured in a previous activity (Zanotti and Gibertini, 2013) for the clean NACA 23012 airfoil at a higher Reynolds number of $1 \cdot 10^6$ indicated that it can be reasonably assumed that the main aerodynamic phenomena are the same at the two Reynolds numbers. Consequently,

the effects due to the L-shaped tab are expected to be similar on the retreating rotor side, as the boundary layer thickness can be considered comparable. Moreover, as for the advancing side of the rotor disk the active device should be controlled in retracted position, apparent effects in terms of drag rise are not expected, as indicated by the steady state simulations performed by Motta et al. (2017) up to $M = 0.7$.

2.1. Test rig

The tests activity was carried out over a NACA 23012 airfoil section model that was object of a detailed experimental investigation about the fine details of dynamic stall process (Zanotti and Gibertini, 2013; Zanotti et al., 2014b). The airfoil model has a $c = 0.3$ m chord and a $b = 0.93$ m span. The aspect ratio of the model is very close to the ones used in the known reference experiments on airfoil dynamic stall (e.g. (Gardner et al., 2011; Leishman, 1990)). As well known, wind tunnel tests of airfoils are affected by sidewalls interference, as the flow rapidly becomes three-dimensional when airfoil stall occurs (Gardner and Richter, 2013). Nevertheless, sidewalls interference should not significantly affect the achievements of the present work aimed to assess the effects of the L-tab by evaluating the differences between the airloads curves measured with and without the active device. In particular, for a proper evaluation of the L-tab effects only, the tests of the clean airfoil were carried out just removing the tab but preserving the actuation system at the model tips.

The model is composed by three aluminium machined section attached to an internal metallic structure. The model central section is equipped with 21 pressure taps positioned along the midspan airfoil contour. The model is pivoted about two external steel shafts with axis at 25% c.

The tests were performed on the oscillating airfoil test rig installed over the wind tunnel test section. The layout of the experimental rig is illustrated in Fig. 1. In particular, the airfoil section model is joined by a shaft to a driving system composed by a brushless servomotor with a 12:1 gear drive. Two different encoders are mounted on the model external shaft, not joined to the motorised strut. In particular, a 2048 *imp/rev* absolute digital encoder with EnDat 2.2 protocol is used for feedback control, while a 4096 *imp/rev* incremental analog encoder is used to get the instantaneous position of the model, thus leading to a measurement accuracy of the model angle of attack less than 0.1°. The model pitching motion is controlled by means of a code implementing a proportional and derivative control. More details about the oscillating airfoil test rig can be found in Zanotti et al. (2011).

2.2. Unsteady pressure measurement set up

The midspan section of the model is instrumented with 21 Kulite miniature fast-response pressure transducers (2 PSI F.S.). The pressure transducers signals were measured by a National Instrument compact data acquisition system equipped with six 24 bit A/D simultaneous bridge modules with 4 channels each. The pressure data from the transducers were collected over 60 complete pitching cycles with a sampling rate

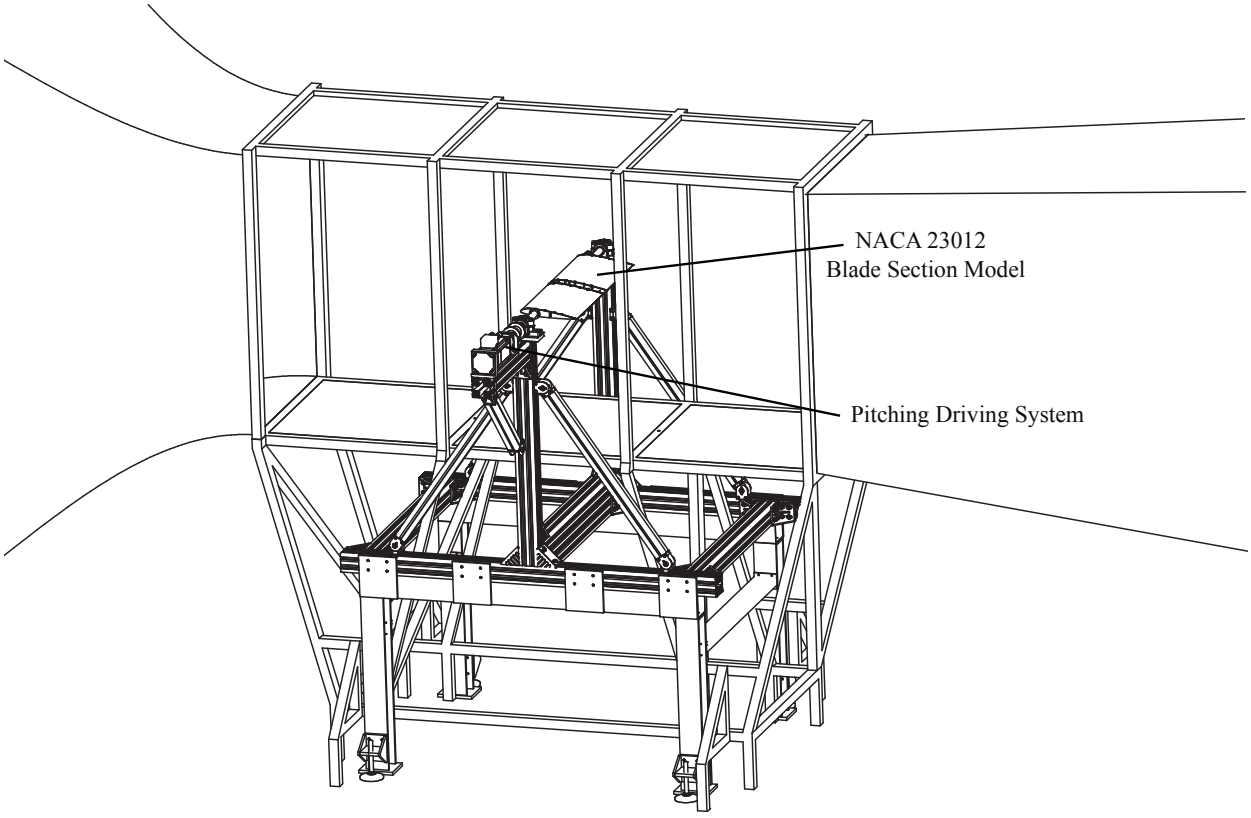

Figure 1: Layout of the oscillating airfoil test rig installed at the *S. De Ponte* wind tunnel of Politecnico di Milano.

of 25 kHz. The lift and pitching moment curves were evaluated by the integration of the phase-averaged pressures measured on the midspan section airfoil contour. The phase-average of the pressure signals was computed using a bin with an amplitude of 0.1° angle of attack. The locations of the pressure taps around the model midspan airfoil contour are listed in Tab. 1 following a closed loop from the upper to the lower surface of the airfoil, starting from the leading edge.

Tap Number	1	2	3	4	5	6	7
Location x/c	0	0.01	0.044	0.096	0.164	0.28	0.358
Tap Number	8	9	10	11	12	13	14
Location x/c	0.453	0.618	0.76	0.9	0.9	0.767	0.628
Tap Number	15	16	17	18	19	20	21
Location x/c	0.459	0.373	0.285	0.185	0.118	0.06	0.02

Table 1: Pressure taps location on the NACA 23012 model midspan section.

The last pressure port on the lower and upper surfaces of the airfoil is located at 90% of the chord, similarly to the airfoil model used by Chandrasekhara et al. (2008, 2004). Indeed, due to feasibility problems

related to their installation, no pressure probes were used at the airfoil trailing edge as well as on the tab. A second order polynomial function interpolating the last three pressure ports signals on the upper or on the lower surface of the airfoil was considered to calculate the pressure at airfoil trailing edge necessary to close the integration in chord. In particular, this value was calculated as the mean of the functions values extrapolated at the airfoil trailing edge position, as done by Chandrasekhara et al. (2008).

An estimation of the airloads calculation accuracy related to the present pressure measurements set up was carried out for the clean airfoil by means of steady state simulations using XFOIL code (Drela and Youngren, 2001). This evaluation shows a maximum error in lift, drag and pitching moment coefficients respectively of 0.021, 0.0015 and 0.002 for $\alpha < 10°$. An estimation of the airloads accuracy related to the lack of pressure information after 90% of the chord was carried out for the airfoil configurations with the L-tab deployed and retracted using the results of steady numerical simulations available from Motta et al. (2017). In fact, the use of a Gurney flap locally modifies the pressure at trailing edge, leading to a rear loading of the airfoil. This flow feature, observed for instance by the measurements carried out by Richter and Rosemann (2002) in steady conditions, is expected to be found also for a pitching airfoil in upstroke before stall onset, as this phase of the motion is characterised by fully attached flow behaviour (McCroskey, 1981; Leishman, 2006). Thus, a reliable indication of the accuracy of the present measurements for flapped configurations should be provided from the results of the simulations performed in pre-stall condition, i.e. $\alpha = 9°$. Indeed, at this same angle of attack a very similar pressure distribution along airfoil contour was measured with the deployed L-tab for steady and unsteady condition in upstroke. The accuracy evaluation shows that for the airfoil configuration with the L-tab deployed the errors in lift, drag and pitching moment coefficients calculation are respectively 0.026, 0.0040 and 0.019. As the error values for lift and drag coefficients are similar to the ones evaluated for the clean airfoil, the accuracy of the pitching moment coefficient is apparently lower. Consequently, the nose-down pitching moment is underestimated in the present measurements. This uncertainty will be taken into account in the discussion of the measured pitching moment curves. On the other hand, for the airfoil configuration with the L-tab retracted the errors in lift, drag and pitching moment coefficients calculation are respectively 0.0045, 0.00046 and 0.003. This error evaluation indicates that, with L-tab retracted, the accuracy of both forces and moment measurements is quite similar to the one obtained for the clean airfoil.

2.3. The active L-shaped tab

The L-shaped tab mounted at the trailing edge region of the airfoil was manufactured from a 1 mm thick steel plate. The tab spans the entire airfoil section model with a 27 mm chord. When deployed, as shown in Fig. 2a, the tab is flush with the airfoil upper surface. Thus, the end prong of the tab behaves essentially as a Gurney flap, even if it is perpendicular to the airfoil upper surface (Liebeck, 1978). Despite the moderate deviation from the 90° mounting angle, a behaviour similar to a classic Gurney flap is expectable,

as supported by Li et al. (2003). In this configuration the end prong of the tab protrudes 4 mm from the trailing edge corresponding to about 1.3% chord of effective height. When retracted, as shown in Fig. 2b, the L-shaped tab features an angle 10.9° with the airfoil upper surface behaving as an upward deflected trailing edge flap.

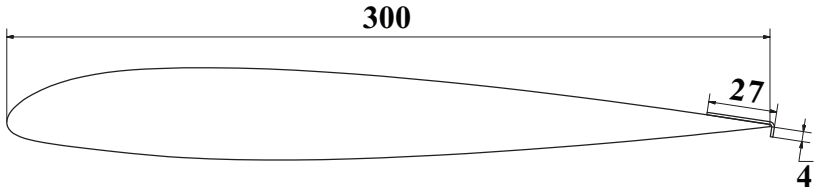

(a) L-tab deployed

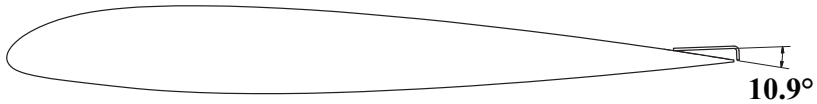

(b) L-tab retracted

Figure 2: L-shaped tab layout at the NACA 23012 airfoil trailing edge (dimensions in mm).

The actuation system of the L-shaped tab is based on the use of two linear pneumatic actuators guided by miniaturized solenoid valves. The actuators consist of pneumatic micro-cylinders with a stroke of 5 mm. As can be observed from the layout shown in Fig. 3a, the actuators were positioned at the tips of the airfoil section model by means of a metallic support. The installation of the actuators at the model tips allowed to avoid any disturbances on the pressure measurements carried out on the model midspan section. The leading edge of the L-shaped tab is attached on the airfoil model upper surface by means of adhesive tape that behaves as a spanwise hinge. Thus, the linear actuators enabled to move the L-tab during the tests in the deployed and retracted positions, as indicated in Fig. 2. The actuation system consists of an open-loop control based on digital input-output boards. In order to move the L-tab in the deployed or retracted position at the selected phase of the pitching cycle, the digital board provides the command signal to the servovalves taking into account the angular position of the model read from the encoder and the time delay between the start of the command signal and the complete displacement of the actuator. This time delay was evaluated by a preliminary measurement made by means of Hall effect sensors (HES), as will be described later. The designed actuation system presents the characteristics to be simple and effective to evaluate the potential capabilities of the investigated device for dynamic stall control. A particular of the mechanical system involved for the L-shaped tab actuation can be observed in Fig. 3b. During the tests, the compressed air was set to 4 bar. More details about the L-shaped tab actuation system are reported in Zanotti et al. (2017).

The use of a 1 mm thick steel plate was dictated by the will to manufacture an L-shaped tab stiff

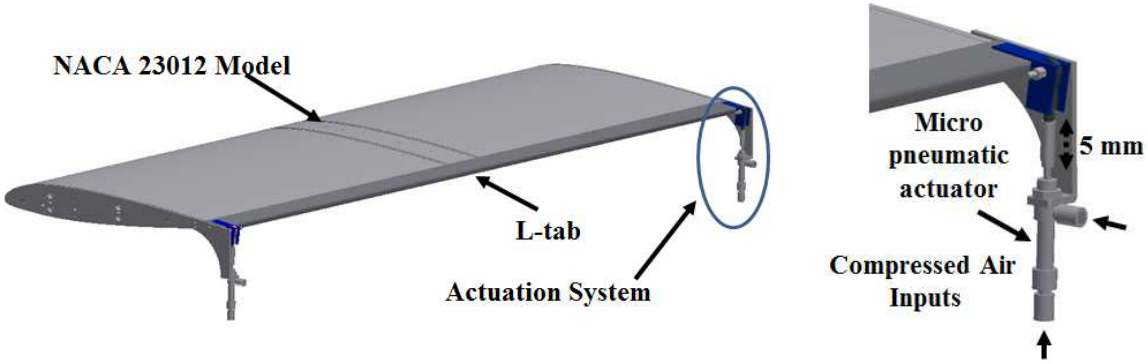

(a) (b)

Figure 3: (a) Layout of the NACA 23012 airfoil section model equipped with the L-shaped tab; (b) particular of the actuation system for the L-shaped tab at the airfoil model tip.

enough to obtain the same deployment of the tab end prong along the entire model span, particularly in correspondence of the instrumented midspan section. The not negligible thickness of the tab could slightly disturb the flow, nevertheless, as confirmed by the obtained tests results, it was not expected that this disturbance could jeopardize the effectiveness of the L-shaped tab for dynamic stall control purpose.

A preliminary analysis of the movement of the L-tab and its response to the command during the pitching cycles investigated in this activity was carried out using two HES mounted on the airfoil lower surface at trailing edge region, respectively in correspondence of the midspan measurement section of the model and on a tip section in correspondence of one actuator. The sketch in Fig. 4a illustrates the HES position on the airfoil section and the magnets position on the tab end prong. The results of these preliminary tests on L-tab movement are reported in Fig. 4b showing the time-history of the height h of the L-tab end prong protruding below the airfoil trailing edge measured by the central and lateral HES and compared to the servovalves command signal. Thus, when the L-tab is completely deployed the measured h would be equal to 4 mm, while when retracted h would be zero (see Fig. 4b). The HES measurements were performed with wind on to consider the real aerodynamic loads acting on the L-tab. In these preliminary tests the L-tab was actuated with a 50% duty cycle that means that the tab was deployed during the whole upstroke and retracted during the whole downstroke motion. For the sake of consistency the HES measurements results are reported only for the pitching cycle with $\alpha_m = 10°$ as the L-tab movement showed an analogous behaviour for the one with $\alpha_m = 15°$.

The HES measurements clearly shows that the L-tab reacts with a constant time delay with respect to the actuation command pulse, used as a parameter in the open-loop control as mentioned earlier. The L-tab

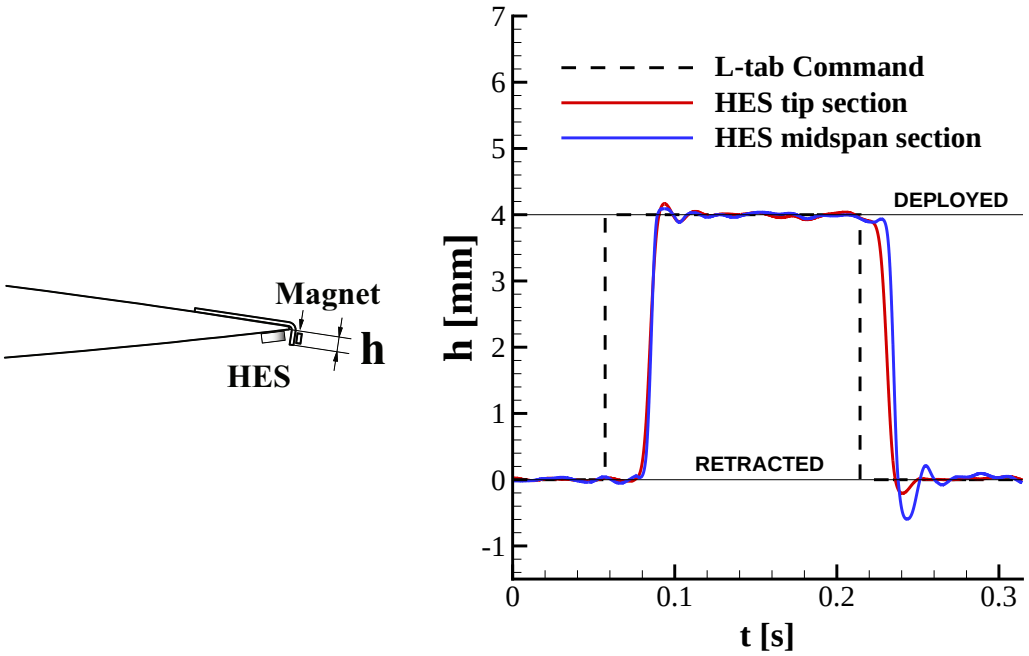

(a) (b)

Figure 4: Preliminary L-tab movement analysis: a) position of the magnet and of the Hall effect sensor (HES) on the airfoil section; b) movement of the L-tab at midspan and tip sections measured by HES with wind on, $\alpha = 10° + 10° \sin(\omega t)$ $U_\infty = 30$ m/s, $k = 0.1$.

reaches the fully deployed and retracted position at the same time instant both at midspan and at the tip section. This confirms the correct functioning of the actuation system. The overshoots observed in the time interval when the L-tab is retracted are related to the elasticity of the hinge and of the tab itself. Indeed, the amplitude of these overshoots measured by the HES at the tip section are much lower due to the higher stiffness of the system closer to the actuation device. Moreover, very small oscillations are also visible from both HES measurement signals in the time interval when the tab is deployed. Of course, the L-tab end prong height h could not feasibly reach values over 4 mm due to the airfoil upper surface presence. Consequently, this behaviour reflects a slight three-dimensional movement of the tab which alters the distance between the magnets on the L-tab and the HES on the airfoil lower surface, thus producing a small error in the evaluation of the tab end prong position. A similar issue was observed in the HES measurements carried out by Gardner et al. (2017) on a pitching airfoil equipped with a back-flow flap.

After the preliminary characterisation of the L-tab movement, the HES at midspan section was removed to avoid disturbances during pressure measurements, while the HES at tip section was preserved to check the correct deployment and retraction of the L-tab at the angles of attack selected for dynamic stall control.

3. Results and discussion

As reported before, the test activity included two deep dynamic stall pitching cycles and different duty cycles for the L-tab actuation. The test matrix of the wind tunnel campaign is reported in Tab. 2. As can be observed, in addition to the test case with the L-tab actuated with 50% duty cycle (Case 1 and 4), the test matrix included test conditions with the L-tab retracted at different angles of attack before the top of the upstroke motion. These attempts are justified by the will to control the peaks of drag and pitching moment due to the deployed tab (acting as a Gurney flap) at stall onset.

Case	α_m	α_a	L-tab Deployed $\alpha-$Interval	L-tab Retracted $\alpha-$range	k	Re	Ma
1	10°	10°	$0° < \alpha < 20°$ upstroke	$20° < \alpha < 0°$ downstroke	0.1	$6 \cdot 10^5$	0.09
2	10°	10°	$0° < \alpha < 18°$ upstroke	18° upstroke $< \alpha < 0°$ downstroke	0.1	$6 \cdot 10^5$	0.09
3	10°	10°	$0° < \alpha < 19°$ upstroke	19° upstroke $< \alpha < 0°$ downstroke	0.1	$6 \cdot 10^5$	0.09
4	15°	10°	$5° < \alpha < 25°$ upstroke	$25° < \alpha < 5°$ downstroke	0.1	$6 \cdot 10^5$	0.09
5	15°	10°	$5° < \alpha < 22°$ upstroke	22° upstroke $< \alpha < 5°$ downstroke	0.1	$6 \cdot 10^5$	0.09
6	15°	10°	$5° < \alpha < 23°$ upstroke	23° upstroke $< \alpha < 5°$ downstroke	0.1	$6 \cdot 10^5$	0.09

Table 2: Pressure measurements test matrix with active L-tab.

A check of the test repeatability was performed for the clean airfoil configuration before the pressure measurements with the active L-tab. The results of the repeatability assessment is presented in Fig. 5 showing the phase averaged lift and pitching moment coefficients curves evaluated in two different wind tunnel runs for both the considered pitching cycles. A quite good repeatability of the phase-averaged airloads coefficients can be observed during all the pitching cycle. Very small discrepancies between the pitching moment curves are visible just in small ranges of angle of attack during downstroke where, as well known, the flow field is characterised by severe unsteadiness due to the passage of large vortical structures (Leishman, 2006; Zanotti and Gibertini, 2013). The high level of unsteadiness in this phase of the pitching motion is also sustained by the standard deviation of the airloads coefficients plotted on the airloads coefficients curves.

3.1. Test results for $\alpha = 10° + 10° \sin(\omega t)$ pitching cycle

3.1.1. Aerodynamic loads analysis

Figure 6 shows the comparison of the phase-averaged airloads coefficients curves evaluated for the pitching cycle characterised by $\alpha_m = 10°$. In order to complete the discussion about the L-tab effects, also the drag coefficient curves, evaluated considering only the pressure contribution, is presented in addition to the lift and pitching moment curves. This further analysis could just provide a preliminary indication about the drag penalty introduced by the tab, taking into account that the measure of the total drag for a deep dynamic

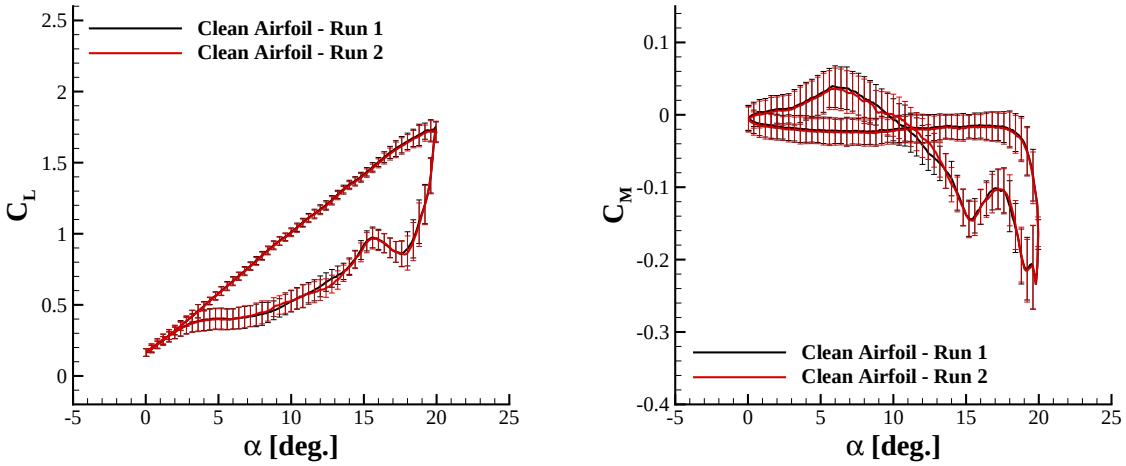

(a) $\alpha = 10° + 10° \sin(\omega t)$ (b) $\alpha = 10° + 10° \sin(\omega t)$

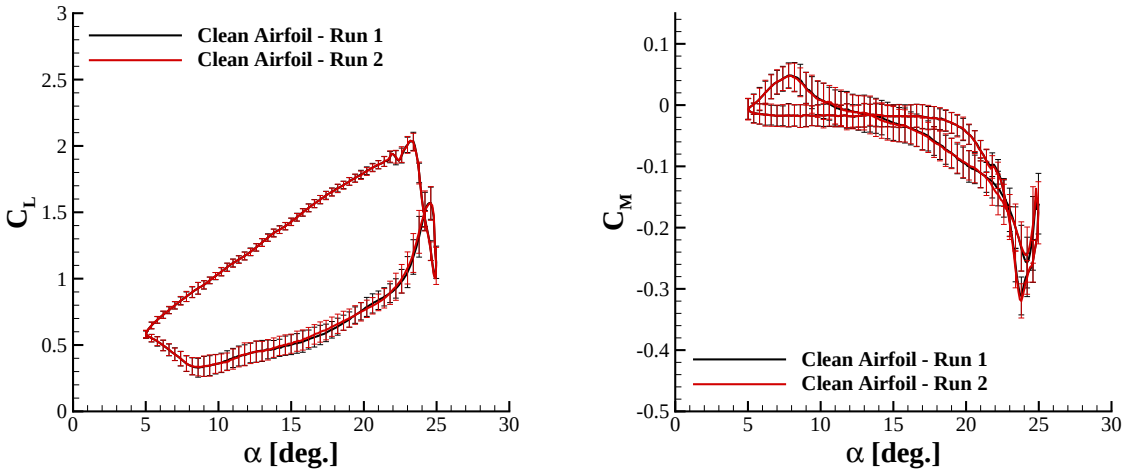

(c) $\alpha = 15° + 10° \sin(\omega t)$ (d) $\alpha = 15° + 10° \sin(\omega t)$

Figure 5: Test repeatability for the lift and pitching moment coefficients curves evaluated for the clean airfoil configuration, $k = 0.1$ ($\mathrm{Re} = 6 \times 10^5$ and $\mathrm{M} = 0.09$) .

stall condition represents, in fact, a very challenging activity due to the severe unsteadiness conditions that characterise this phenomenon.

A more accurate evaluation of the active control performance on airloads peaks were performed by calculating the average of all individual cycle peaks, as described in Ramasamy et al. (2016). Indeed, the airloads peaks found from the phase-averaged data can underestimate the values occurring on individual cycles, as they could occur at different angles of attack over the set of pitching cycles considered for the measurements. In particular, Fig. 7 shows the comparison of the average of all individual cycle airloads

peaks (with 1σ bar in both α and peak magnitude) normalised for the phase-averaged value evaluated for the clean airfoil case. The figure also include the phase-averaged peak values of the airloads coefficients evaluated for the clean and active controlled test cases. The peak values obtained for case 2 are not presented for a better readability of Fig. 7.

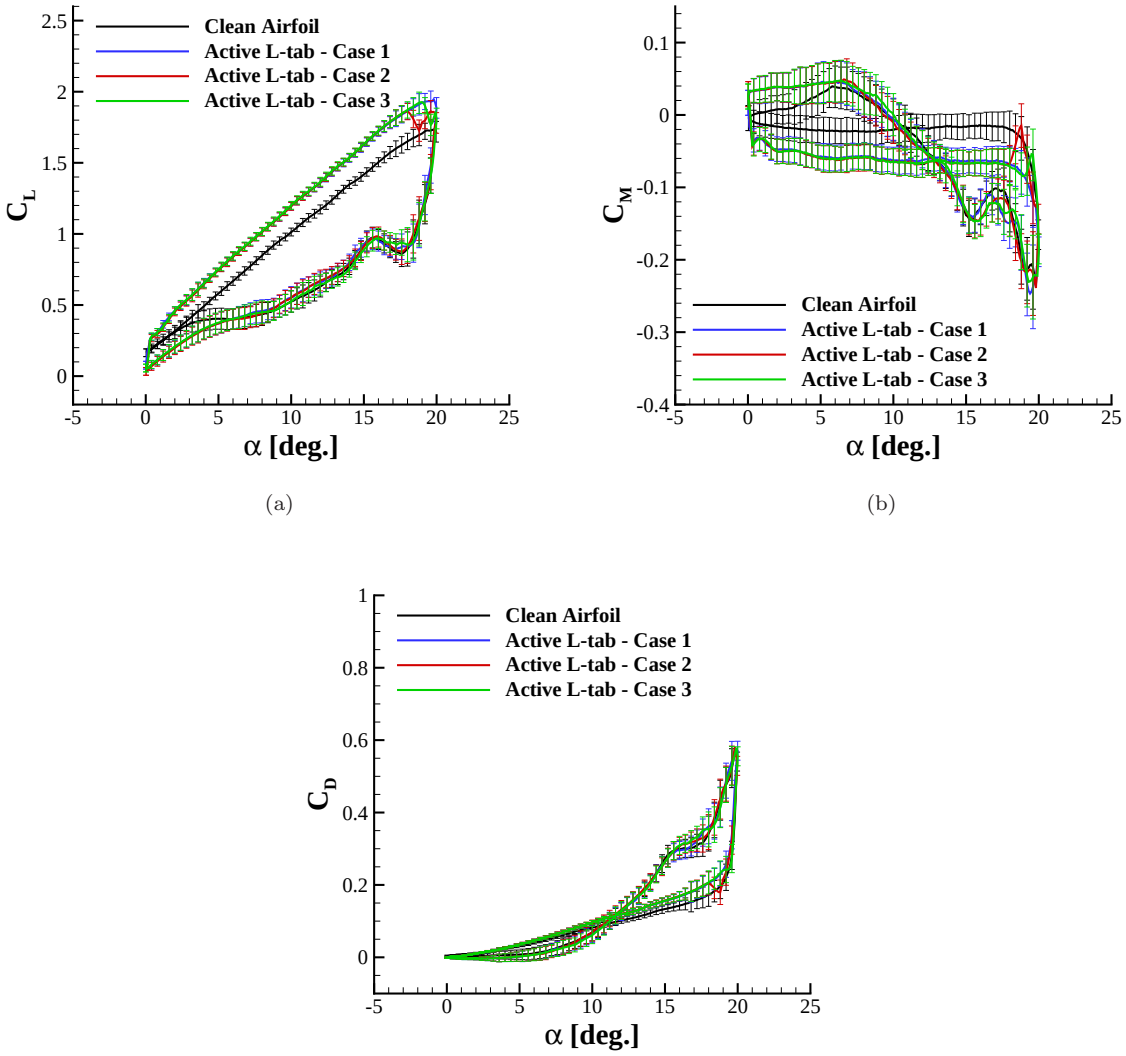

(a) (b)

(c)

Figure 6: Comparison of the phase-averaged airloads curves measured for $\alpha = 10° + 10° \sin(\omega t)$, $k = 0.1$ ($\mathrm{Re} = 6 \times 10^5$ and $\mathrm{M} = 0.09$).

Tests results show that the deployed L-shaped tab generates in upstroke an apparent increase of lift with respect to the clean airfoil configuration, analogously to what observed by Chandrasekhara et al. (2008) for a pitching VR-12 airfoil equipped with a Gurney flap at the trailing edge (see Fig. 6a). The observed

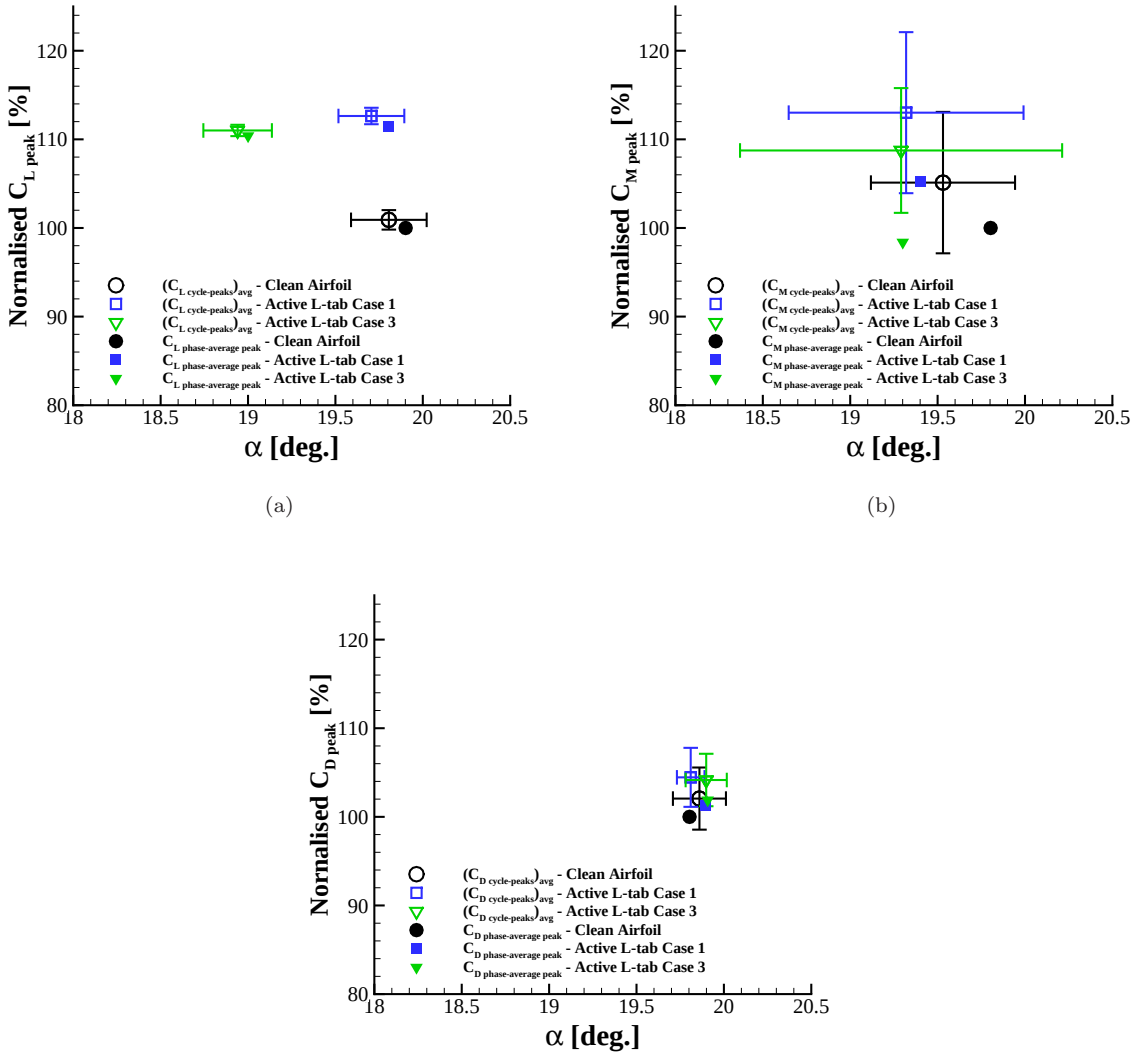

Figure 7: Comparison of the average of all individual cycle airloads peaks against phase-average values for $\alpha = 10° + 10° \sin(\omega t)$, $k = 0.1$ (Re $= 6 \times 10^5$ and M $= 0.09$).

increase of lift occurring deploying the L-tab in upstroke can be an important benefit for an helicopter rotor blade due to the associated higher level of available thrust very useful on the retreating side of the rotor disk at high advance ratio. In particular, the peak analysis reported in Fig. 7a shows for test case 1 an increase of the lift coefficient phase-averaged peak of about 12% with respect to the clean airfoil case. The amount of phase-averaged C_L peak increase is similar to the one evaluated considering the average of the individual cycle peaks, as for the present test condition, the scatter of C_L peaks is very small. Indeed, it is worth noting that the phase-averaged C_L peak value falls within 1σ variation of the average of all individual

cycle C_L peaks.

The pitching moment curves comparison shows that for test case 1 the deployment of the L-shaped tab up to the maximum incidence of the upstroke introduces a downward shift of the curve (see Fig. 6b). Consequently, the load level on the pitch-link would remarkably increase, taking also into account the results of the accuracy evaluation of the pitching moment measurements carried out for the airfoil configuration with the L-tab deployed. In particular, a more severe pitching moment peak is introduced for the controlled test case 1, as can be observed from the peak analysis shown in Fig. 7b. The retraction of the L-tab before the stall onset does not produce a valuable effect in terms of pitching moment peak reduction. Indeed, both retracting the tab at $\alpha = 18°$ (case 2) or at $\alpha = 19°$ (case 3) in upstroke, almost the same pitching moment peak measured for the clean airfoil is obtained. This issue should be explained by the fact that the L-tab, being a trailing edge device, has a limited effect on the vortical structures typical of deep dynamic stall regime, generated by leading edge separations and responsible for pitching moment stall. Nevertheless, the shift-down of the pitching moment curves combined with the not altered peak of C_M provides an apparent reduction of the amplitude of the pitching moment breakdown at stall with respect to the clean case. This apparent reduction of the pitching moment transient could be considered a valuable effect for the blade command chain.

In particular, the correct evaluation of C_M peaks carried out averaging the individual cycle peaks shows that the C_M peak for case 3 is just slightly higher than the clean one. It is worth noting that the scatter of C_M peaks is higher than the C_L one, as pitching moment peaks occur at the beginning of downstroke where the flow is highly unsteady. Moreover, analogously to what observed by Ramasamy et al. (2016), for the controlled test case 3 the phase-averaged peak of C_M underestimates the average of individual cycle peaks by about 10% (see Fig. 7b).

A partial indication on drag issue related to the use of the active device is given by the comparison of the measured pressure drag contribution. The comparison of the phase-averaged curves shown in Fig. 6c indicates a contained pressure drag penalty with respect to the clean airfoil case just during upstroke when the L-tab is deployed. The peak analysis in Fig. 7c shows a very small increase of the C_D peak for the active controlled cases with respect to the clean condition and a very small scatter of the C_D peak in both directions for all the test cases.

Due to the lack of the viscous drag term, a definite performance assessment of the investigated active device was not possible. Nevertheless, the present measurements confirm that higher lift to drag values can be obtained with a deployable Gurney flap near stall, as achieved by the measurements carried out by Richter and Rosemann (2002). Indeed, the comparison of the phase-averaged C_D curves shows that the pressure drag penalty introduced by the L-tab decreases for increasing angle of attack in upstroke. Moreover, in proximity of the maximum angle of attack reached during the pitching cycle, the percent increase of the average of all individual cycle C_L peaks obtained for controlled case 3 is higher than the C_D one.

Generally speaking, the phase-averaged airloads coefficients curves evaluated when the L-tab is retracted retrace quite well the behaviour of the clean airfoil ones, as almost all the downstroke phase of the motion is characterised by fully separated flow. An exception can be observed in the low incidence part of the downstroke where the flow is reattached. Indeed, in this portion of the cycle the lift coefficient measured with the retracted tab is lower that the clean airfoil one (see Fig. 6a), thus indicating that the retracted tab behaves like a slightly upward deflected flap.

3.1.2. Aerodynamic damping analysis

The aerodynamic damping characteristics were analysed by evaluating the time-resolved aerodynamic damping coefficient based on the Hilbert transform of the pitching moment time-series measured throughout the pitching cycle. This analysis offers a thorough insight into the mechanism of transient stall flutter onset. In particular, the transient aerodynamic damping coefficient, defined in Bowles et al. (2012) as

$$\Xi(t) = -\frac{A_{C_M}(t)}{\alpha_a} \sin\left(\arctan\left(\frac{\tilde{C_M}}{C_M}\right) - \omega t\right), \tag{1}$$

was calculated for each test case and compared in Fig. 8 to the corresponding values of the cycle-integrated aerodynamic damping coefficient defined in Carta (1967) as

$$\Xi_{cycle} = -\frac{\oint C_M d\alpha}{\pi \alpha_a^2}. \tag{2}$$

The time-resolved damping curve evaluated for the clean airfoil shows a region of positive damping in the first half of upstroke motion. Then, the damping becomes negative reaching a minimum value in correspondence of the top of the upstroke, where also the negative peak of the C_M is reached. This negative damping augmentation is due to the formation, growth and migration of vortical structures typical of deep dynamic stall regime. In particular, two confined negatively-damped portions of the curve can be observed around the two local negative peaks of the pitching moment. These regions could promote the occurrence of high-frequency stall flutter divergence from the rotor control input (Bowles et al., 2012). The aerodynamic damping then returns to positive values during downstroke as the flow is fully reattaching. The time-resolved damping evaluated for the cases with active controlled L-tab shows a positive shift of the curves occurring during the upstroke when the tab is deployed. This produces a delay of the passage to negative damping values and the consequent reduction of the amplitude in α of the negatively-damped portion of the curve. Moreover, the minimum value of the damping is reduced for the active controlled test cases with respect to the clean airfoil case. In particular a maximum reduction of about 30% of the negative damping peak is obtained for test case 1. A similar effect is observed in terms of reduction of the secondary local negative damping peak occurring in downstroke motion. In addition, the last portion of downstroke motion

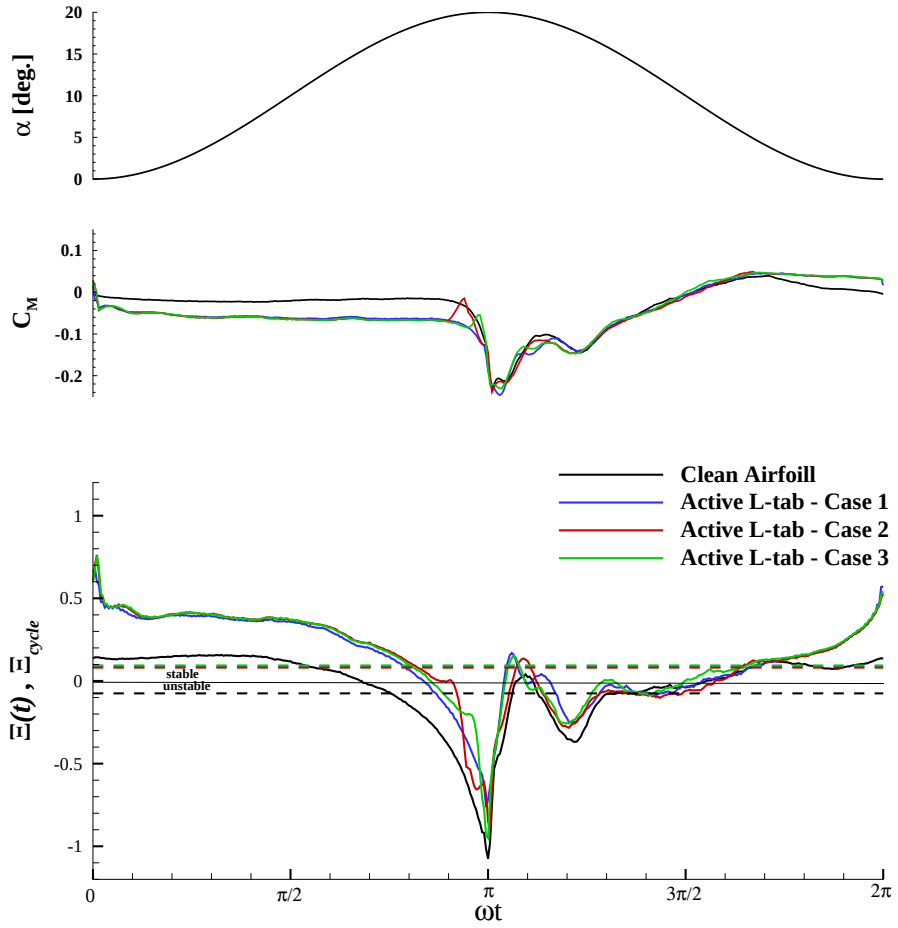

Figure 8: Transient aerodynamic damping analysis for $\alpha = 10° + 10° \sin(\omega t)$, $k = 0.1$ (Re $= 6 \times 10^5$ and M $= 0.09$). The dashed lines represent the corresponding cycle-integrated aerodynamic damping.

is characterised by higher positive values of damping for the active controlled cases with respect to the clean airfoil case.

It is worth noting that the cycle-integrated damping calculated for the clean airfoil is negative (see dashed lines in Fig. 8), as can be clearly deduced by the larger clockwise loop area of the $C_M - \alpha$ curve with respect to the anti-clockwise loop area (see Fig. 6b). On the other hand, a quite positive value of the cycle-integrated aerodynamic damping coefficient is obtained for all the three test cases with active controlled L-tab, as the clockwise loop area of the $C_M - \alpha$ curves is apparently reduced, while the anti-clockwise loop area is enlarged with respect to the clean airfoil test condition. Consequently, the active controlled L-tab introduced an apparent valuable effect, considering the cycle-integrated perspective, on aerodynamic damping. Nevertheless, the time-resolved damping analysis shows that negatively-damped portions of the pitching cycle remain for the active controlled test cases, even if their amplitude and the negative damping

peaks are reduced with respect to the clean airfoil case. As previously mentioned, the destabilising effect associated to negative damping is due to the the formation of vortical structures generated by leading edge flow separations. Thus, a trailing edge device as the investigated L-tab has not particular effect on this feature. Consequently, this consideration suggests the use of a leading edge device in addition to the active L-tab. Indeed, as shown by Chandrasekhara et al. (2008), this solution would enable to combine the lift enhancement effect produced by a Gurney flap and the alleviation of the pitching moment peaks due to the formation of strong vortical structures, thus avoiding this destabilising effect of the dynamic stall process.

3.1.3. Pressure distribution analysis

Some considerations about physical interpretation of the active L-tab functioning can be deduced from the comparison of pressure coefficient distributions reported in Fig. 9 for some selected angles of attack along the pitching cycle. In this figure, the clean airfoil pressure distribution is always compared with the measurements of a single controlled test case to provide a better readability of the results. The standard deviations of the measured C_P are plotted on the curves.

The comparison between the $-C_P$ distribution measured for the clean airfoil at $\alpha = 16°$ in upstroke and the one measured for the controlled case 1 (see Fig. 9a) enables to evaluate the effect of the deployed tab. The lift increase introduced deploying the L-shaped tab is, in fact, related to both a higher suction (lower pressure) on the airfoil upper surface and to a higher pressure on the lower surface. In particular, a higher local pressure increase can be observed at lower surface trailing edge region due the flow slowing down at the forward facing side of the tab end prong. These effects are typical of Gurney flaps (Kinzel and Maughmer, 2010).

An overall view for the physical interpretation of the lift coefficient increase due to the deployed tab is given by the comparison of the C_P surface distribution measured in the whole upstroke motion reported in Fig. 10. Indeed, for the controlled case 1 the peak pressures over the airfoil upper surface are higher and spread over a larger angles of attack range, as indicated by $\Delta\alpha$ representing the range where the $-C_P$ contour levels are above 5.

The C_P comparison at $\alpha = 18.8°$ in upstroke shows the effect of the L-tab retraction by comparison of the measurements carried out for the controlled case 2. In particular, the pressure distribution behaviour measured with the L-tab retracted is very close to the clean airfoil pressure distribution with only exception on the airfoil upper surface at trailing edge region where a local effect due to the tab presence is apparent (see Fig. 9b).

The C_P distribution measured at $\alpha = 19.7°$ in downstroke for the controlled case 3 indicates that the retracted tab produces a local higher pressure on the airfoil upper surface at trailing edge region and a lower local pressure at leading edge region (see Fig. 9c).

At $\alpha = 15.8°$ in downstroke the flow field on the airfoil upper surface is fully separated and dominated

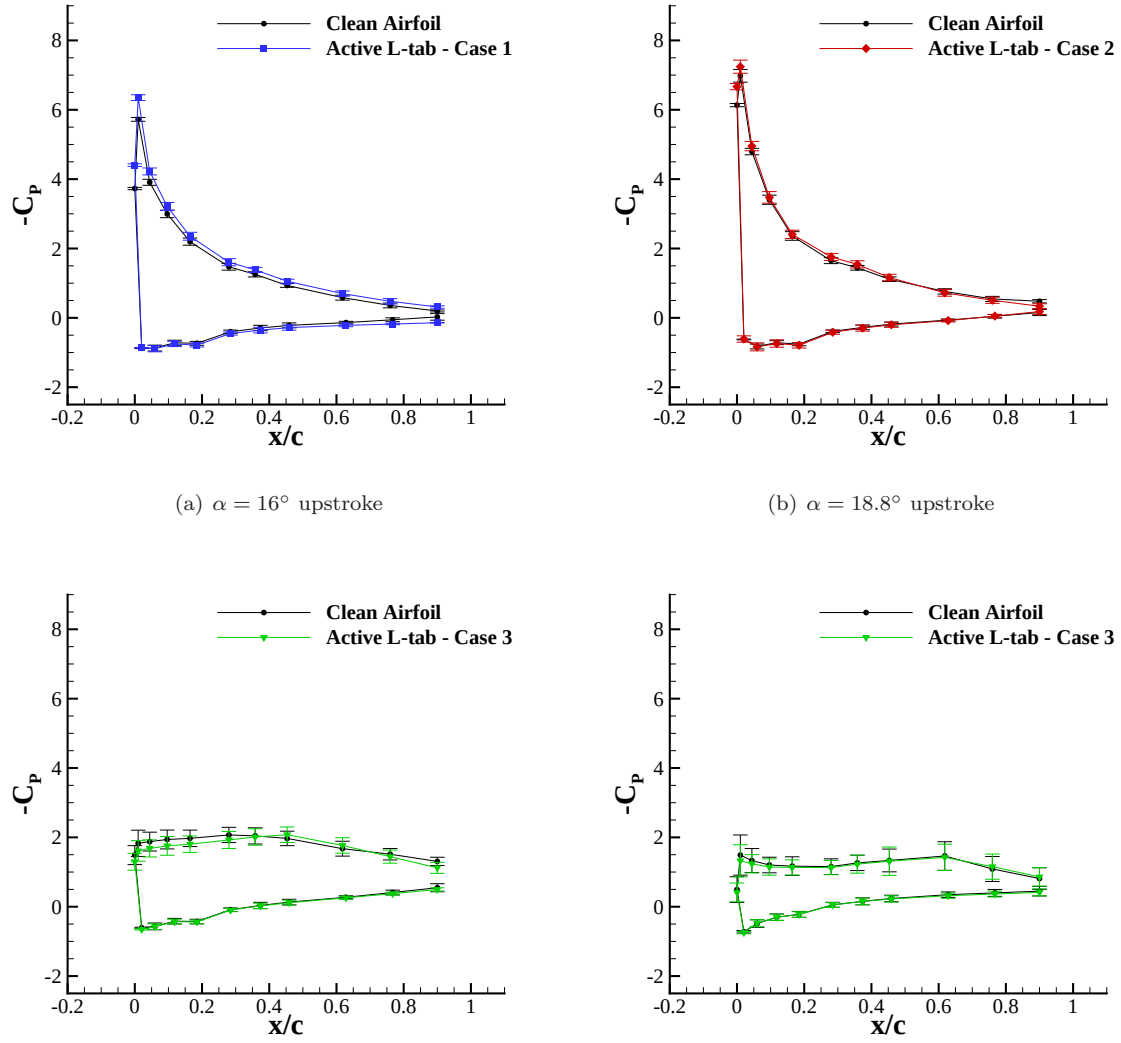

(a) $\alpha = 16°$ upstroke

(b) $\alpha = 18.8°$ upstroke

(c) $\alpha = 19.7°$ downstroke

(d) $\alpha = 15.8°$ downstroke

Figure 9: Comparison of the pressure coefficient distributions measured for $\alpha = 10° + 10° \sin(\omega t)$, $k = 0.1$ ($\mathrm{Re} = 6 \times 10^5$ and $\mathrm{M} = 0.09$).

by the formation of large vortical structures, as indicated by the overshoots of the lift and pitching moment coefficients curves (see Fig. 6a and b). Thus, the retracted trailing edge L-tab at this phase of the motion does not have appreciable effects on these structures, as shown by the C_P distribution comparison reported in Fig. Fig. 9d.

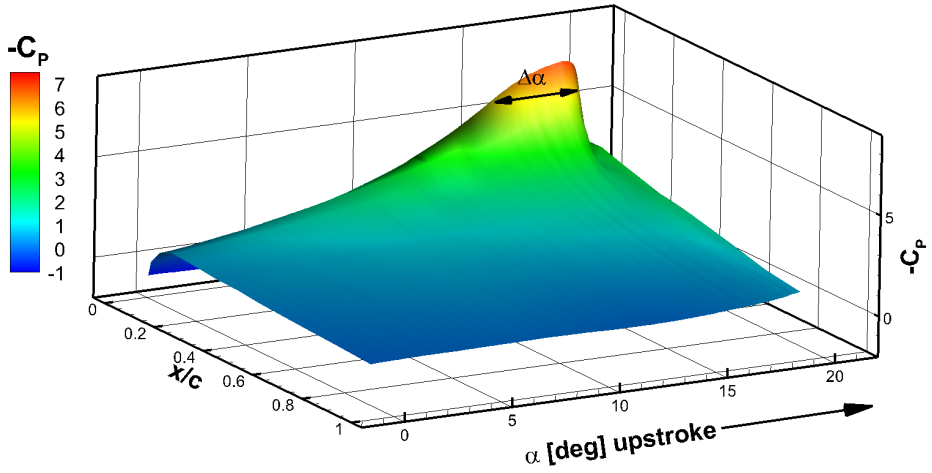

(a) Clean Airfoil

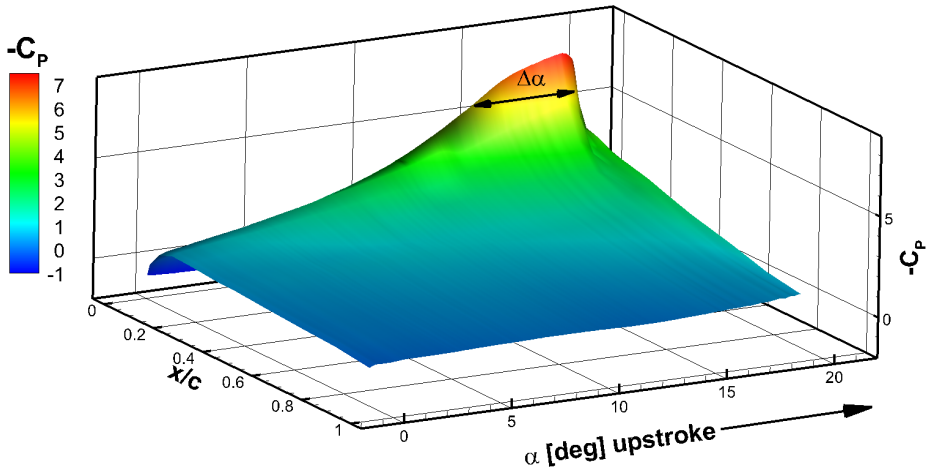

(b) Active L-tab - Case 1

Figure 10: Comparison of the pressure coefficient surface distributions measured on the airfoil upper surface for $\alpha = 10° + 10° \sin(\omega t)$ in upstroke, $k = 0.1$ ($\mathrm{Re} = 6 \times 10^5$ and $\mathrm{M} = 0.09$).

3.2. Test results for $\alpha = 15° + 10° \sin(\omega t)$ pitching cycle

3.2.1. Aerodynamic loads analysis

Figure 11 shows the comparison of the phase-averaged airloads coefficients curves evaluated with and without the active controlled L-tab for the pitching cycle with $\alpha_m = 15°$. This pitching cycle, characterised by a mean angle of attack close to the airfoil static stall angle of attack, is a case of deep dynamic stall regime (McCroskey, 1981). Indeed, the lift coefficient curve measured for the clean airfoil configuration shows a typical non-linear change of its slope in the last portion of the upstroke, due to the formation and migration on the airfoil upper surface of the DSV (see Fig. 11a). Analogously to what observed from the

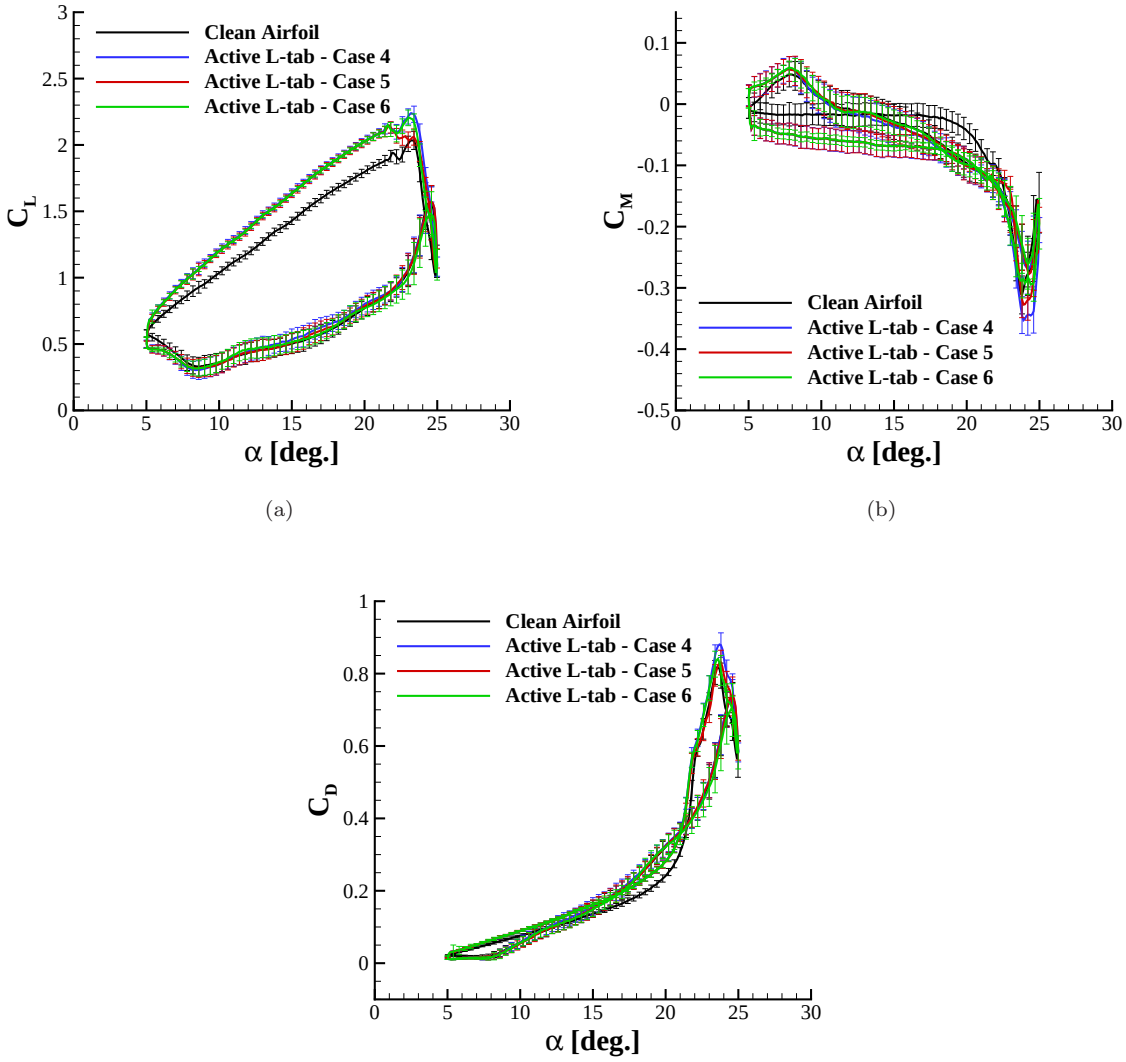

Figure 11: Comparison of the phase-averaged airloads curves measured for $\alpha = 15° + 10° \sin(\omega t)$, $k = 0.1$ ($\mathrm{Re} = 6 \times 10^5$ and $\mathrm{M} = 0.09$).

results obtained for the pitching cycle characterised by $\alpha_m = 10°$, the deployed tab introduces an apparent increase of lift with respect to the clean airfoil configuration. In particular, the peak analysis reported in Fig. 12a shows an increase of the C_L peak of about 10% for test case 4. Moreover, a higher scatter of the C_L peak in α was observed for the present pitching cycle due to the fact that the lift peaks occur in the portion of the cycle characterised by the DSV passage.

Concerning the pitching moment curves comparison, analogously to what found for the previous investigated pitching cycle, the controlled case 4 results show a more severe negative pitching moment peak with

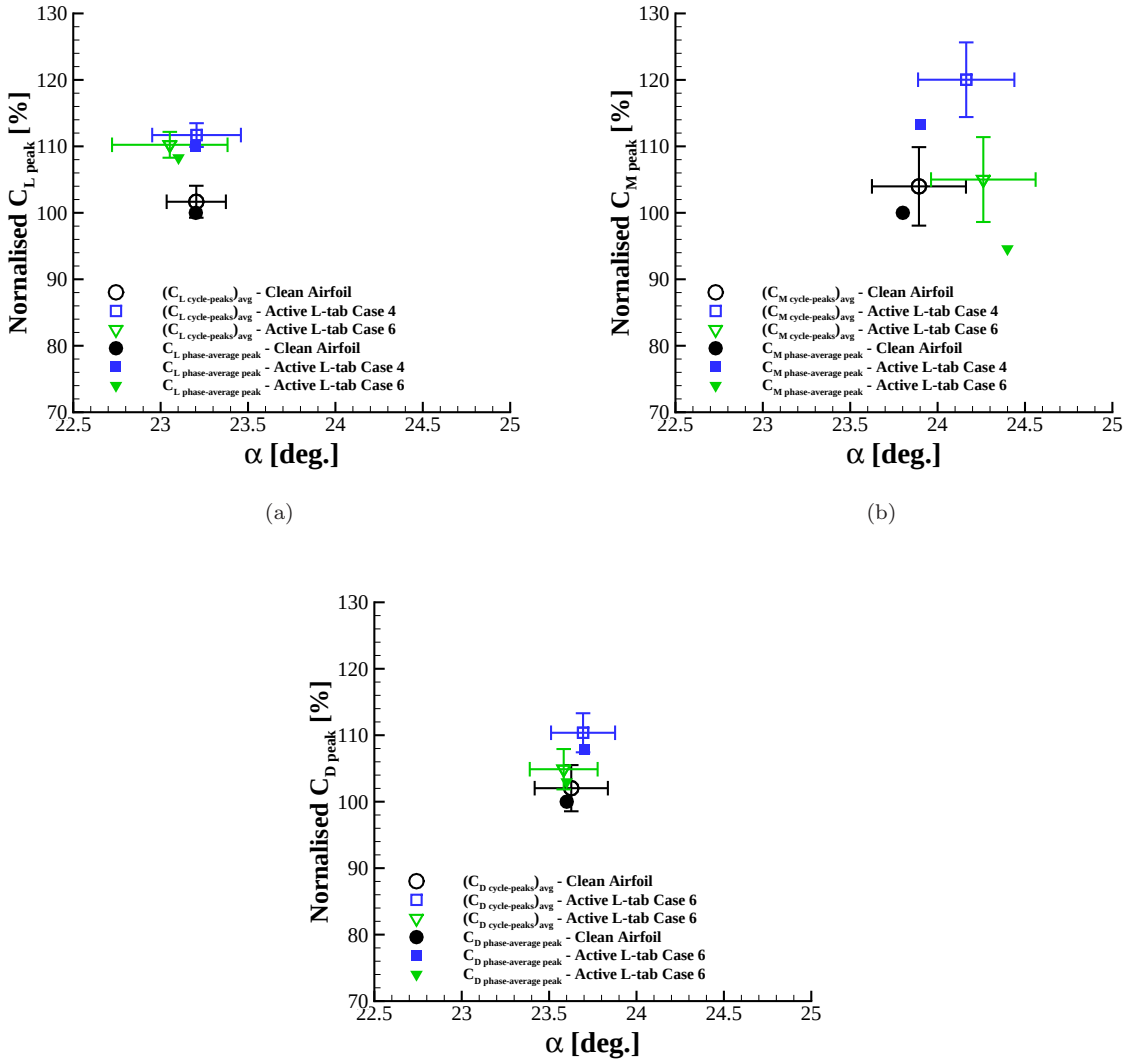

Figure 12: Comparison of the average of all individual cycle airloads peaks against phase-average values for $\alpha = 15° + 10° \sin(\omega t)$, $k = 0.1$ ($\mathrm{Re} = 6 \times 10^5$ and $\mathrm{M} = 0.09$).

respect to the clean airfoil and a shift downward of the pitching moment curve up to the moment stall incidence occurring at about 22°. Retracting the L-tab at $\alpha = 22°$ (case 5) in upstroke, just before the onset of the DSV formation, produces a drop of the lift and a consequent reduction of the lift breakdown. Retracting the L-tab at $\alpha = 23°$ in upstroke (case 6) at the end of the DSV , slightly alters the behaviour of the lift curve and of the maximum lift coefficient achieved for this test case with respect to the controlled case 4. On the other hand, the negative pitching moment peak value is practically unaffected with respect to the clean airfoil. Indeed, acting at the trailing edge region of the airfoil, the active L-tab or Gurney flap

is not effective for pitching moment peak alleviation compared to other leading edge devices investigated in literature (e.g. Chandrasekhara et al. (2004); Gardner et al. (2013)) that strongly influence the DSV process responsible of the pitching moment breakdown. The peak analysis reported in Fig. 12b shows that the phase-average underestimates the pitching moment peak, thus providing a bad evaluation of the L-tab performance (Ramasamy et al., 2016). Indeed, the correct evaluation of C_M peaks carried out averaging the individual cycle peaks shows that for case 6 the C_M peak is very close to the clean one. Nevertheless, also for this pitching cycle a large decrease of the amplitude of the pitching moment breakdown at stall is obtained (about 25% for test case 6). This issue leads to an apparent reduction of the amplitude of the rapid loads variation acting on the pitch-link.

Concerning the phase-averaged pressure drag curves analysis, also for this pitching cycle, the deployed L-tab introduces a contained pressure drag penalty with the peak occurring at stall for the active controlled cases (see Fig. 11c). Retracting the L-tab before stall onset (case 6) the drag peak resumes roughly the same value of the clean airfoil configuration and the pressure drag penalty results to be negligible at high incidences (see Fig. 12c). Thus, as previously discussed for the pitching cycle with $\alpha_m = 10°$, an improvement of blade efficiency is expected at higher incidences during dynamic stall process phase.

3.2.2. Aerodynamic damping analysis

The comparison of the time-resolved and cycle-integrated aerodynamic damping analysis for this second deep dynamic stall pitching cycle is shown in Fig. 13.

Analogously to what found for pitching cycle with $\alpha_m = 10°$, the deployed L-tab produces a positive shift of the time-resolved damping curve occurring in upstroke up to the stall onset. Consequently, the negatively-damped portion of the curve, occurring in correspondence of the phase of the upstroke motion characterised by the migration of the DSV, is reduced. Moreover, an apparent reduction of the negative minimum of the damping is obtained for the active controlled test cases. In particular, a decrease of about 40% of the clean airfoil peak of negative damping is observed for test case 6.

Once the DSV detached from the airfoil at the top of the upstroke motion, a rapid augmentation to positive damping values is observed for all the test cases. Then, a secondary local negative damping peak occurs at the beginning of downstroke for the clean airfoil case. The reduction of this local peak obtained with the active L-tab produces positive damping values, particularly high for test case 4. Nevertheless, a wide portion of downstroke is characterised by negative damping up to the fully flow reattachment occurring at low angles of attack, when the damping coefficient returns to positive values. In this phase of the motion, the retracted L-tab has a negligible effect of the negatively-damped portion of the curves.

The cycle-integrated damping perspective masks the occurrence of these negatively-damped portions of the curves, as, for the present pitching cycle, the net aerodynamic damping evaluated for the clean airfoil has a slight positive value. The active L-tab control produces, similarly to what found for the pitching cycle

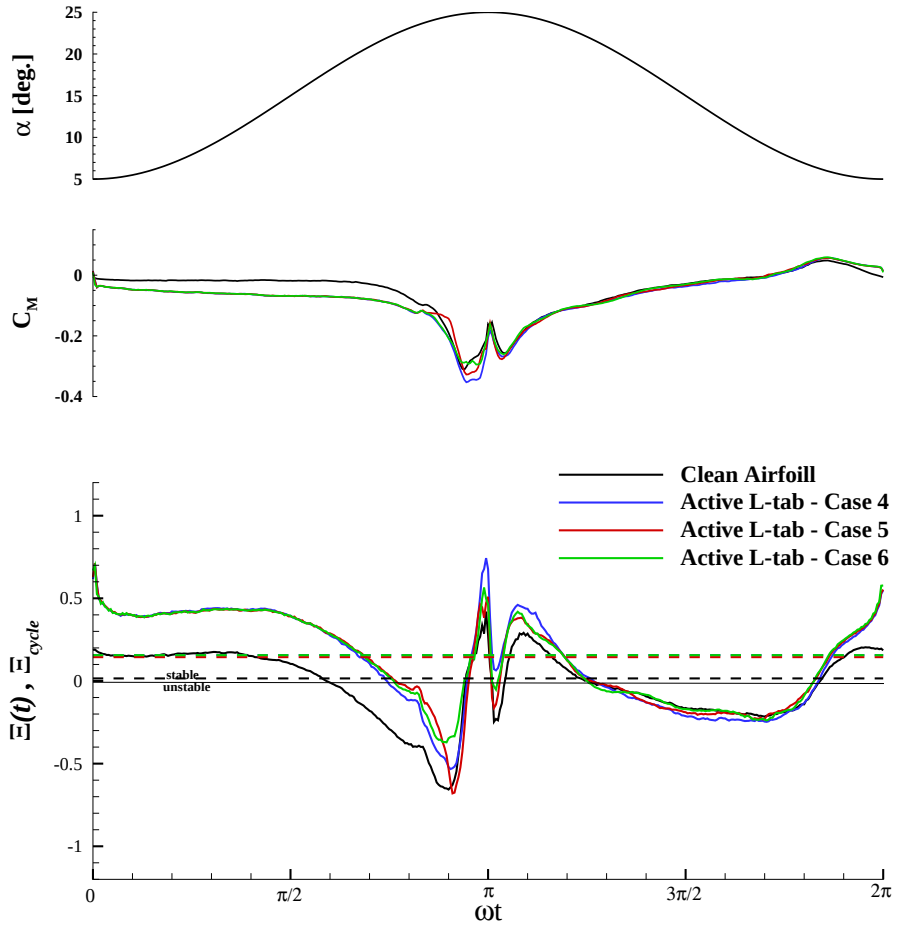

Figure 13: Transient aerodynamic damping analysis for $\alpha = 15° + 10° \sin(\omega t)$, $k = 0.1$ (Re $= 6 \times 10^5$ and M $= 0.09$). The dashed lines represent the corresponding cycle-integrated aerodynamic damping.

with $\alpha_m = 10°$, an increase of the counter-clockwise loop areas of the pitching moment curve (see Fig. 11). In particular, for all the three controlled test cases, this effect is quite apparent, as the positive value of the cycle-integrated aerodynamic damping coefficient in increased tenfold with respect to the clean airfoil value.

3.2.3. Pressure distribution analysis

Further insight about the effect of the L-tab on flow behaviour can be deduced from pressure distribution comparisons reported in Fig. 14. The $-C_P$ distribution measured for the clean airfoil at $\alpha = 18.4°$ in upstroke shows that the flow at this incidence, well beyond the static stall angle of attack, is still attached to the airfoil upper surface due to the effect of induced camber increase produced by the rapid positive pitching rate (Leishman, 2006). The pressure coefficient distribution comparison with the controlled case 4 reported in Fig. 14a confirms at this phase of the motion the effect of lift increase introduced by the L-tab deployment, due to a higher suction on the upper surface and to a higher pressure on the lower surface.

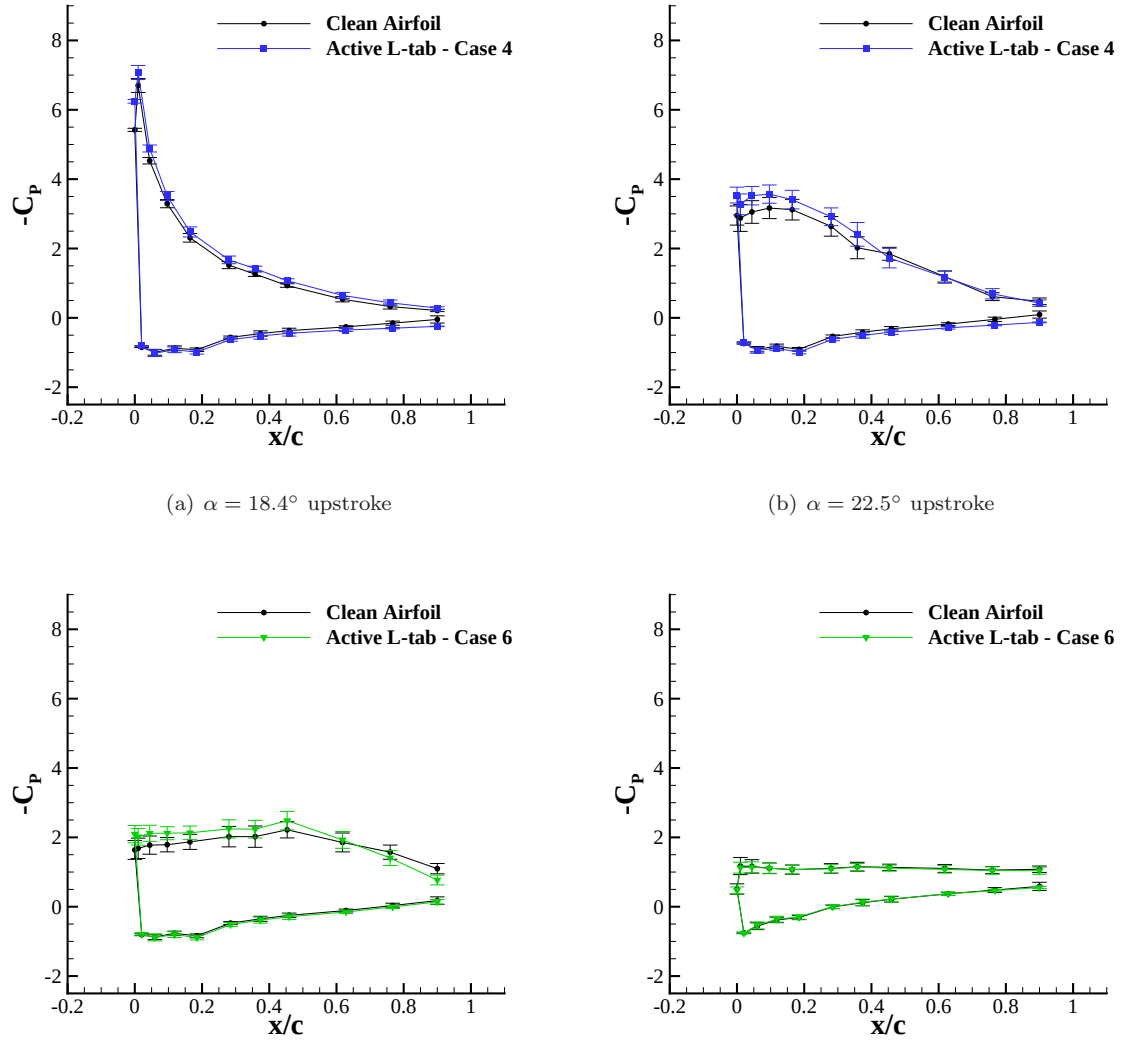

(a) $\alpha = 18.4°$ upstroke

(b) $\alpha = 22.5°$ upstroke

(c) $\alpha = 23.8°$ downstroke

(d) $\alpha = 16°$ downstroke

Figure 14: Comparison of the pressure coefficient distributions measured for $\alpha = 15° + 10° \sin(\omega t)$, $k = 0.1$ ($\mathrm{Re} = 6 \times 10^5$ and $\mathrm{M} = 0.09$).

The $-C_P$ distribution measured for the clean airfoil at $\alpha = 22.5°$ in upstroke shows the typical features produced by DSV formation. In particular, at this phase of the motion a drop of the suction peak at leading edge region is apparent showing that the flow is already largely separated. For the clean airfoil condition the suction on the airfoil upper surface is generally lower with respect to the controlled case 4 except for a local peak around midchord that represents the fingerprint of a vortex structure (DSV) travelling over the airfoil (see Fig. 14b). An overall insight on the L-tab effect on the DSV can be achieved from the comparison of the C_P surface distribution measured in the whole upstroke motion reported in Fig. 15. In

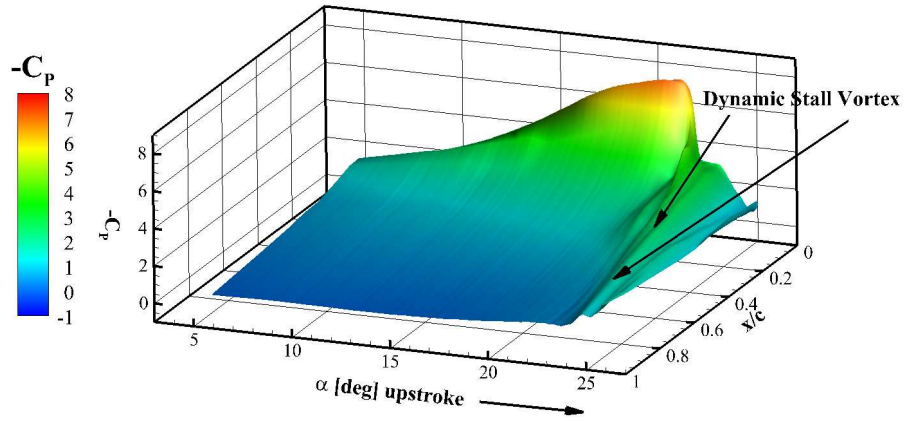

(a) Clean Airfoil

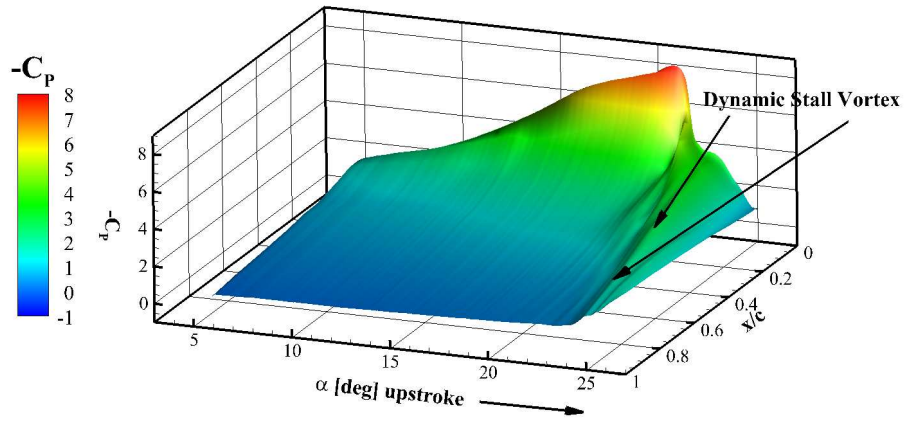

(b) Active L-tab - Case 4

Figure 15: Comparison of the pressure coefficient surface distributions measured on the airfoil upper surface for $\alpha = 15° + 10° \sin(\omega t)$ in upstroke, $k = 0.1$ ($\mathrm{Re} = 6 \times 10^5$ and $\mathrm{M} = 0.09$).

particular, the footprint of the DSV passage on the clean airfoil upper surface is clearly visible from the local rising suction peak present in the last portion of the upstroke motion, indicated by arrows in Fig. 15a. The surface pressure distribution measured for controlled case 4 in the same portion on the motion shows a scarce flattening of this surface pressure elevation (see Fig. 15b).

At $\alpha = 23.8°$ in upstroke the DSV has left the airfoil and the flow on the airfoil upper surface is fully separated as can be observed by $-C_P$ distribution measured for the clean airfoil (see Fig. 14c). For the controlled case 6 the L-tab produces a modification of the upper surface pressure distribution, particularly a local higher pressure at trailing edge region.

Analogously to what observed for the pitching cycle with $\alpha - m = 10°$, the downstroke motion is characterised by a fully stalled flow behaviour. Thus the L-tab has negligible effects on pressure distribution,

as can be observed by the $-C_P$ comparison measured at $\alpha = 16°$ in downstroke shown in Fig. 14d.

4. Conclusions

The performance of a trailing edge active L-shaped tab for dynamic stall control was assessed by means of a wind tunnel campaign carried out on a pitching airfoil in deep dynamic stall conditions. In particular, unsteady pressure measurements were carried out to evaluate by integration the sectional aerodynamic loads loops acting on the NACA 23012 airfoil at midspan. Moreover, the comparison of the local pressure distributions measured along the airfoil chord enabled to achieve a description of the local effects on the airfoil contour due to the L-tab functioning.

Tests results showed that the deployment of the tab during almost the whole upstroke motion produces, similarly to what occurs by the use of a Gurney flap, a conspicuous increase of lift corresponding to a higher level of available thrust on the retreating blade of a helicopter rotor in fast forward flight. Nevertheless, a shift down of the pitching moment curve was also introduced by the tab deployed in attached flow conditions. Retracting the tab before the stall onset and during the whole downstroke motion did not introduce a valuable effect on the peak of the pitching moment, as it was almost returned back to the value measured for clean airfoil. On the other hand, a conspicuous reduction of the amplitude of the pitching moment breakdown at stall was observed.

The time-resolved damping analysis shows that the active device produces an increase of the positive damping values in the attached flow regions of the pitching cycles. Moreover, a reduction of the amplitude of the negatively-damped portions of the pitching cycles and of the minima of the negative damping values with respect to the clean airfoil case are observed for the active controlled cases. Nevertheless, these negatively-damped portions are not avoided with the active L-tab control as, being a trailing edge device, it produces a limited result on the vortical structures issued from leading edge at stall that are responsible for this destabilising effect. Thus, the present results indicated that a smart solution for dynamic stall control on a blade would be the combination of a leading edge device, producing a valuable effect on pitching moment peaks alleviation, with a deployable Gurney flap producing a lift enhancement effect.

Generally speaking, the present measurements indicated the benefits and limits of the use of a deployable Gurney flap for dynamic stall control on a pitching airfoil. As a matter of fact, due to the limits of the 2D pitching airfoil approach (higher Mach number on advancing blade) and to some limitations of the measurement set up (viscous drag term not evaluable), a definite performance assessment related to the use of a deployable Gurney flap on a helicopter blade in realistic flight conditions could not be deduced from the present results. Nevertheless, the aim of the present work was to show a smart solution to integrate a deployable Gurney flap, widely investigated in literature, at blade trailing edge. Indeed, thanks to its design, the investigated device exhibits the suitability to be installed easily on helicopter blades as the tab

could be easily integrated on the blade external surface. Moreover, the use of appropriate solutions for its actuation (e.g. pneumatic muscle actuators or piezo-electric actuators) would avoid the problem of weight rise that is particularly severe under high centrifugal loads.

Acknowledgements

The authors would acknowledge Donato Grassi for his support to the wind tunnel activity.

References

Bowles, P., Coleman, D., Corke, T., Thomas, F., Wasikowski, M., 2012. Compressibility effects on aerodynamic damping during dynamic stall events, AHS 68th Annual Forum, 1–3 May, Forth Worth, TX, USA.

Carta, F.O., 1967. An analysis of the stall flutter instability of helicopter rotor blades. Journal of the American Helicopter Society 12, 1–8.

Chandrasekhara, M., Martin, P., Tung, C., 2004. Compressible dynamic stall control using a variable droop leading edge airfoil. Journal of Aircraft 41, 862–869.

Chandrasekhara, M., Martin, P., Tung, C., 2008. Compressible dynamic stall performance of a variable droop leading edge airfoil with a gurney flap. Journal of the American Helicopter Society 53, 18–25.

Drela, M., Youngren, H., 2001. XFOIL 6.94 User Guide. Cambridge, MA.

Feszty, D., Gillies, E., Vezza, M., 2004. Alleviation of airfoil dynamic stall moments via trailing-edge flap flow control. AIAA Journal 42, 17–25.

Gardner, A., Richter, K., Mai, H., Altmikus, A.R.M., Klein, A., Rohardt, C.H., 2011. Experimental investigation of dynamic stall performance for the edi-m109 and edi-m112 airfoils, 37th European Rotorcraft Forum, 13–15 September, Gallarate (VA), Italy.

Gardner, A.D., Opitz, S., Wolf, C.C., Merz, C.B., 2017. Reduction of dynamic stall using a back-flow flap. CEAS Aeronautical Journal 8, 271–286.

Gardner, A.D., Richter, K., 2013. Effect of the model-sidewall connection for a static airfoil experiment. Journal of Aircraft 50, 677–680.

Gardner, A.D., Richter, K., Mai, H., Neuhaus, D., 2013. Experimental investigation of air jets for the control of compressible dynamic stall. Journal of the American Helicopter Society 58, 1–14.

Kentfield, J.A.C., 1993. The potential of gurney flaps for improving the aerodynamic performance of helicopter rotors, AIAA International Powered Lift Conference, AIAA Paper 93-4883.

Kinzel, M.P., Maughmer, M.D., 2010. Numerical investigation on the aerodynamics of oscillating airfoils with deployable gurney flaps. AIAA Journal 48, 1457–1469.

Le Pape, A., Costes, M., Richez, F., Joubert, G., David, F., Deluc, J.M., 2012. Dynamic stall control using deployable leading-edge vortex generators. AIAA Journal 50, 2135–2145.

Leishman, J.G., 1990. Dynamic stall experiments on the naca 23012 aerofoil. Experiments in Fluids 8, 49–58.

Leishman, J.G., 2006. Principles of helicopter aerodynamics. Cambridge Aerospace series.

Li, Y., Wang, J., Zhang, P., 2003. Influences of mounting angles and locations on the effects of gurney flaps. Journal of Aircraft 40, 494–498.

Liebeck, R.H., 1978. Design of subsonic airfoils for high lift. Journal of Aircraft 15, 547–561.

Mai, H., Dietz, G., Geissler, W., Richter, K., Bosbach, J., Richard, H., de Groot, K., 2008. Dynamic stall control by leading edge vortex generators. Journal of the American Helicopter Society 56, 26–36.

Maughmer, M.D., Bramesfeld, G., 2008. Experimental investigation of gurney flaps. Journal of Aircraft 45, 2062–2067.

McCroskey, W.J., 1981. The Phenomenon of Dynamic Stall. NASA TM 81264.

Motta, V., Zanotti, A., Gibertini, G., Quaranta, G., 2017. Numerical assessment of an l-shaped gurney flap for load control. Proceedings of the Institution of Mechanical Engineers, Part G: Journal of Aerospace Engineering 231, 951–975.

Pisetta, G., 2016. Verifica sperimentale degli effetti di un gurney flap attivo su un profilo oscillante in regime di stallo dinamico (English: Experimental verification of the effects of a gurney flap on an oscillating airfoil in dynamic stall). Master's thesis. Politecnico di Milano.

Post, M., Corke, T., 2006. Separation control using plasma actuators: Dynamic stall vortex control on oscillating airfoil. AIAA Journal 44, 3125–3135.

Ramasamy, M., Wilson, J.S., McCroskey, W.J., Martin, P.B., 2016. Measured characteristics of cycle-to-cycle variations in dynamic stall, AHS Technical Meeting on Aeromechanics Design for Vertical Lift, 20–22 January, San Francisco, CA, USA.

Richter, K., Rosemann, H., 2002. Experimental investigation of trailing-edge devices at transonic speeds. The Aeronautical Journal 106, 185–193.

Singh, C., Peake, D., Kokkalis, A., Khodagolian, V., Coton, F., Galbraith, R., 2006. Control of rotorcraft retreating blade stall using air-jet vortex generators. Journal of Aircraft 43, 1169–1176.

Woodgate, M.A., Pastrikakis, V.A., Barakos, G.N., 2016. Method for calculating rotors with active gurney flaps. Journal of Aircraft 53, 605–626.

Yee, K., Joo, W., Lee, D.H., 2007. Aerodynamic performance analysis of a gurney flap for rotorcraft application. Journal of Aircraft 44, 1003–1014.

Yeo, H., 2008. Assessment of active controls for rotor performance enhancement. Journal of the American Helicopter Society 53, 152–163.

Zanotti, A., Auteri, F., Campanardi, G., Gibertini, G., 2011. An experimental set up for the study of the retreating blade dynamic stall, 37th European Rotorcraft Forum, 13–15 September, Gallarate (VA), Italy.

Zanotti, A., Gibertini, G., 2013. Experimental investigation of the dynamic stall phenomenon on a naca 23012 oscillating aerofoil. Proceedings of the Institution of Mechanical Engineers, Part G: Journal of Aerospace Engineering 227, 1375–1388.

Zanotti, A., Grassi, D., Gibertini, G., 2014a. Experimental investigation of a trailing edge l-shaped tab on a pitching airfoil in deep dynamic stall conditions. Proceedings of the Institution of Mechanical Engineers, Part G: Journal of Aerospace Engineering 228, 2371–2382.

Zanotti, A., Grassi, D., Pisetta, G., Gibertini, G., 2017. Experimental evualuation of an active controlled l-shaped tab for dynamic stall alleviation, 43th European Rotorcraft Forum, Milan, Italy.

Zanotti, A., Nilifard, R., Gibertini, G., Guardone, A., Quaranta, G., 2014b. Assessment of 2d/3d numerical modeling for deep dynamic stall experiments. Journal of Fluids and Structures 51, 97–115.